



# NiO/ZnO heterojunction nanorod catalyst for high-efficiency electrochemical conversion of methane

Cheolho Kim, Heewon Min, Junmin Kim, Jiwon Sul, Jiwoo Yang, Jun Hyuk Moon\*

Department of Chemical and Biomolecular Engineering, Institute of Emergent Materials, Sogang University, 35 Baekbeom-ro, Mapo-gu, Seoul 04107, Republic of Korea

## ARTICLE INFO

### Keywords:

Electrocatalyst  
Methane conversion  
Heterojunction catalyst  
Core/shell nanorod

## ABSTRACT

Electrochemical conversion is promising for selective partial oxidation of methane. We present a NiO/ZnO shell/core nanorod catalyst used to enhance electrochemical conversion. The built-in potential at the NiO/ZnO interface and the 1D morphology of the nanorods allow for fast charge transfer, thereby enhancing electrochemical methane conversion. We achieved a high ethanol production rate of 1084.2  $\mu\text{mol/g}_{\text{NiO}}/\text{hr}$  with a selectivity of 81 % for a 600-nm long NiO/ZnO nanorod catalyst. Mechanistic analyses with isotopic labeling reactions suggested ethanol production pathways involving generation of active oxygen by dissociative adsorption of the anionic  $\text{CO}_3^{2-}$  oxidant, formation of methanol by methane activation, and coupling of deprotonated methanol and methane. Furthermore, we improved the ethanol yield by improving methane solubility in sulfolane cosolvent mixtures. We also demonstrated conversion with in situ generation of  $\text{CO}_3^{2-}$  from a  $\text{CH}_4/\text{CO}_2$  mixture.

## 1. Introduction

Methane is an abundant resource due to the development of shale gas and also a greenhouse gas with a global warming potential 25 times that of  $\text{CO}_2$  [1]. Efficient and environmentally friendly utilization of methane is urgent and indispensable [2,3]. The large dissociation energy of the methane C–H bond requires high temperatures for oxidation reactions; these conditions lead to favorable oxidation of intermediates, resulting in poor selectivity for partial oxidation [4–7]. Currently, commercial conversion of methane into high value-added chemicals relies on an indirect method using syngas, and it requires high energy consumption because the process temperature ranges within 700–1100 °C [8–11].

Many studies have been focused on the development of catalytic processes for partial oxidation of methane at low temperatures. In particular, inspired by the enzyme monooxygenase that converts methane to methanol at room temperature, various zeolite catalysts containing iron or copper (e.g., Fe-ZSM-5, Cu-ZSM-5, Cu-MOR, Cu-SSZ-13, etc.) have been developed [12]. They have achieved conversion of methane to alcohols (mainly methanol) in the temperature range 125–200 °C with molecular oxygen or  $\text{N}_2\text{O}$  as oxidizing agents. However, these processes still require temperature-varying multistep processes with a high-temperature step for activation of the catalyst [13, 14].

Electrochemical methane conversion for partial oxidation of methane under ambient conditions is attracting attention [15–19]. This approach generates active oxygen species (e.g.,  $\text{OH}^*$  and  $\text{O}^*$ ) by applying electrochemical potentials instead of thermal energy and enhances the catalytic activity by controlling the Madelung potential of the catalyst [8,20]. In addition, solvation by the liquid medium stabilizes reaction intermediates and extracts the product immediately [21,22]. These distinct advantages allow for continuous partial oxidation of methane at a constant temperature. In their pioneering work, Mustain and coworkers demonstrated room temperature electrochemical conversion of methane to various oxygenates, including  $\text{CH}_3\text{OH}$ ,  $\text{C}_2\text{H}_5\text{OH}$ ,  $\text{HCHO}$  and  $\text{CH}_3\text{COCH}_3$ , on NiO-based catalysts [15]. Sun and coworkers demonstrated electrochemical methane-alcohol conversion by employing NiO/Ni catalysts; they achieved a production rate of 25  $\mu\text{mol/g}_{\text{NiO}}/\text{hr}$  with selectivities of 77 % for ethanol and 23 % for methanol [16]. Zheng and coworkers achieved methane-ethanol conversion with a Rh/ZnO nanosheet catalyst exhibiting a production rate of 789  $\mu\text{mol/g}_{\text{cat}}/\text{hr}$  [17].

In electrochemical conversions, the electrical properties of the catalyst may have a significant effect on the reaction rate. Active oxygen species are formed electrochemically by oxidation of water or dissociation of electrolyte salts; furthermore, it has been confirmed that the methane-alcohol conversion route includes an electrochemical reaction

\* Corresponding author.

E-mail address: [junhyuk@sogang.ac.kr](mailto:junhyuk@sogang.ac.kr) (J.H. Moon).

<https://doi.org/10.1016/j.apcatb.2022.122129>

Received 9 June 2022; Received in revised form 11 October 2022; Accepted 28 October 2022

Available online 10 November 2022

0926-3373/© 2022 Elsevier B.V. All rights reserved.

step [16,23,24]. The effects of catalyst charge transport properties have already been demonstrated in the electrochemical reduction of  $\text{CO}_2$  or in the electrochemical oxidation of water [25,26]. Xiao and coworkers have demonstrated enhancement of electrochemical  $\text{CO}_2$  reduction by using the p-n heterojunction catalyst  $\text{Zn}_2\text{SnO}_4/\text{SnO}_2$  [25]. Wang and coworkers improved the efficiency of water splitting by exploiting the p-n heterojunction catalyst MnCo carbonate-hydroxide/NiFe-hydroxide [26]. These heterojunction catalysts achieve fast reaction kinetics with charge transport facilitated by the potential built-in across the junction. Nevertheless, electrochemical catalysts for methane conversion with controlled charge transport have not yet been explored and thus remain an urgent challenge.

In this study, we present a NiO/ZnO shell/core nanorod catalyst for electrochemical methane conversion. Previously, NiO catalysts have been applied to complete oxidation of methane; the Ni atom binds the  $\text{CH}_3$  intermediate favorably [27]. NiO exhibits high activity for oxidative dehydrogenation of ethane [28]. In addition, ZnO substrates have been widely applied in electrochemical and photoelectrochemical devices due to their high electron mobilities as well as availability with various morphologies [29]. Our NiO/ZnO nanorods are designed to enhance electrochemical reactions on the NiO catalyst surface by vectorial charge diffusion through one-dimensional nanorods as well as fast charge transport due to the built-in potential of the heterojunction (Fig. 1). Electrochemical methane oxidation with NiO/ZnO nanorod catalysts produces ethanol as the main product. A reaction employing isotopes confirmed the formation of ethanol by a reaction of methane with oxygen in the  $\text{CO}_3^{2-}$  oxidant. DFT calculations identified a thermodynamically favorable pathway for production of ethanol, which consisted of methane activation by  $\text{O}^*$ , deprotonation of methanol, and coupling to methane. By controlling the length of the nanorod catalyst, we confirmed that the highest ethanol productivity occurred with the 600 nm-long NiO/ZnO nanorod catalyst. The production rate for ethanol reached  $1084.2 \mu\text{mol/g}_{\text{NiO}}/\text{hr}$  with a selectivity of 81 %; this performance is superior to those of previous electrochemical catalysts. Furthermore, we demonstrated enhancement of the methane conversion by facile methane dissolution with a sulfolane cosolvent and conversion via generation of in situ  $\text{CO}_3^{2-}$  oxidant by using a practical  $\text{CH}_4/\text{CO}_2$  mixed gas.

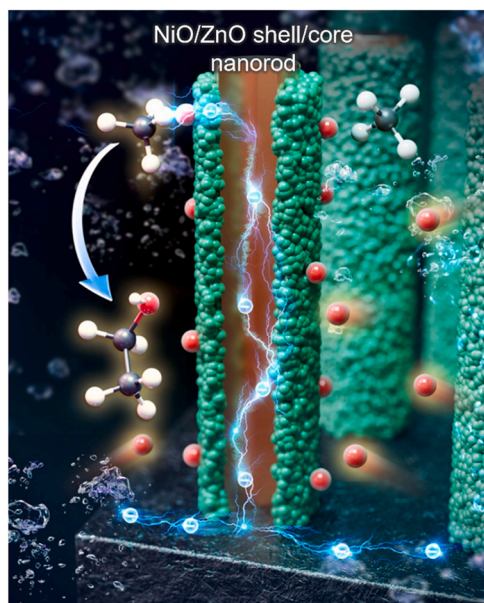


Fig. 1. Scheme for promoting methane-ethanol conversion by fast electron diffusion in NiO/ZnO shell/core nanorod catalysts.

## 2. Experimental

### 2.1. Preparation of NiO/ZnO nanorod catalyst

ZnO nanorods were prepared by a hydrothermal reaction on a carbon cloth substrate. A mixture of 25 mM  $\text{Zn}(\text{NO}_3)_2 \cdot 6\text{H}_2\text{O}$  and 25 mM  $\text{C}_6\text{H}_{12}\text{N}_4$  was prepared. The reaction proceeded in an autoclave reactor at  $90^\circ\text{C}$ . The lengths of the nanorods were controlled with reaction time ranging from 1 to 10 hr. The NiO shell on the surface of the nanorods was coated by reaction with a mixed solution of 1 M  $\text{NiSO}_4 \cdot 0.6\text{H}_2\text{O}$ , 0.25 M  $\text{K}_2\text{S}_2\text{O}_8$  and  $\text{NH}_4\text{OH}$ . Heat treatment at  $550^\circ\text{C}$  for 1 hr produced the NiO/ZnO shell/core nanorods.

### 2.2. Electrochemical methane conversion

Cyclic voltammetry (CV) curves were measured using a conventional three-electrode system. A catalyst-coated carbon cloth substrate ( $1 \times 1 \text{ cm}^2$ ) was used as the working electrode, Pt as the counter electrode, and a saturated calomel electrode (SCE) as the reference electrode. An aqueous solution containing 0.5 M  $\text{Na}_2\text{CO}_3$  was used as the electrolyte. The voltammograms were recorded with a potentiostat (Versastat, Ametek); the scan rate was 0.02 V/s. The electrochemical impedance spectrum (EIS) was recorded with an impedance analyzer (Versastat, AMETEK); the frequency was scanned in the range 0.1 Hz – 1 MHz, and the voltage amplitude was set to 10 mV. For electrochemical methane oxidation, the electrolyte was saturated with methane by bubbling methane for 30 min. The electrochemical methane conversion was carried out in a gas-tight reactor in which the catalyst electrode and the Pt counter electrode were immersed. The electrochemical potential was applied with a potentiostat (Versastat Ametek).

### 2.3. Isotopic analyses

$^{13}\text{CH}_4$  was purchased from Sigma—Aldrich (99 %, 99 atom %  $^{13}\text{C}$ ). The conversion reaction was carried out with  $^{13}\text{CH}_4$ -saturated  $\text{D}_2\text{O}$ . For synthesis of the  $^{18}\text{O}$ -labeled carbonate, first,  $[^{18}\text{O}]$  water (200  $\mu\text{L}$ , 9.1 mmol, 98 %  $^{18}\text{O}$ ) was reacted with tetraethyl orthocarbonate (5 mL, 23.8 mmol) and toluenesulfonic acid (dehydrated, 1.5 mg). After a few minutes of reaction, a solution of 500 mM sodium methoxide in dry methanol (30 mL, 15 mmol) and  $[^{18}\text{O}]$  water (350  $\mu\text{L}$ , 15.9 mmol) was added. This mixed solution was heated at  $80\text{--}85^\circ\text{C}$  for 30 hr. Removal of the solvent using a rotary evaporator yielded an  $^{18}\text{O}$ -labeled sodium carbonate precipitate. The conversion reactions with isotopes utilized  $\text{D}_2\text{O}$  as the solvent.  $^{13}\text{C}$  NMR spectra were recorded with an Avance III HD 400 FT NMR instrument (Bruker Biospin); the proton high-power decoupling field strength was 11.7 (5.0  $\mu\text{s}$  length  $90^\circ$   $^1\text{H}$  pulse). The contact time was 4 ms at the Hartmann-Hahn matching condition of 50 kHz, and the scan delay time was 3 s. The  $^{13}\text{C}$  chemical shift of the product was analyzed to an accuracy of  $\pm 0.5$  ppm. Tetramethylsilane (TMS) was applied as an external standard. The measurement was calibrated through the residual signal of 3-(trimethylsilyl)-1-propane sulfonic acid sodium salt (DSS) at  $\delta = 0.0$  ppm.

### 2.4. Product analyses

Gas chromatography (7820 A, Agilent Technologies, USA) with a flame ionization detector (FID) and a PoraPLOT Q column was used for product analyses. The injection temperature was set to  $250^\circ\text{C}$ . For the FID, a flow of 300 mL/min Ar, 40 mL/min  $\text{H}_2$  fuel, and 25 mL/min  $\text{N}_2$  make-up was applied. The oven temperature was programmed to set an initial temperature of  $40^\circ\text{C}$ , ramp for 2 min to  $80^\circ\text{C}$  ( $20^\circ\text{C}/\text{min}$ ), and then to  $230^\circ\text{C}$  ( $30^\circ\text{C}/\text{min}$ ). Gas chromatography-mass spectra were recorded with a gas chromatograph (GC—MS, 7890B-5977A, Agilent Technologies, USA) equipped with an MSD 5975 mass selective detector (electron impact ionization, EI, 70 eV, Agilent Technologies). A fused-silica capillary (DB-WAX, 0.5  $\mu\text{m}$  thick poly(ethylene glycol) coating,

Agilent Technologies, USA) was used as the column. The sample was injected by head space sampling (1000  $\mu\text{L}$  of sample heated at 75–80  $^{\circ}\text{C}$  for 45 min); the injection temperature was 250  $^{\circ}\text{C}$ . Helium (1 mL/min, 99.999 %) was used as the carrier gas; the dilution ratio was 10:1 (sample:He). The oven temperature programmed for 5 min at 40  $^{\circ}\text{C}$ , 4  $^{\circ}\text{C}/\text{min}$  to 100  $^{\circ}\text{C}$  and 3 min at 240  $^{\circ}\text{C}$  (20  $^{\circ}\text{C}/\text{min}$ ).

## 2.5. Characterization

SEM and TEM images were recorded with a JSM-7800 F (JEOL) and a JEM-4300 (JEOL), respectively. XRD data was obtained with a Rigaku Miniflex-2005G303 X-ray diffractometer (Cu K $\alpha$  radiation at 20 kV and 10 mA) in the 2  $\theta$  range of 25–65 $^{\circ}$ . XPS data were recorded with a Leybold photoelectron spectrometer (Al K $\alpha$  monochromatic beam). UV–Vis spectra were measured using a Shimadzu UV-2550

spectrophotometer with an ultraviolet–visible diffuse reflection spectroscope. UPS data were recorded with an ultraviolet photoelectron spectrometer (NEXSA XPS, Thermo Fisher Scientific) with He I radiation (21.2 eV) and an energy resolution of 0.05 eV.

## 2.6. DFT calculations

All calculations were performed using the Quantum ESPRESSO package based on density functional theory with the Hubbard-U framework (DFT+U). For the calculations, the projector augmented (PAW) method and the Generalized gradient approximation (GGA) with the Perdure-Burke-Ernzerhof (PBE) exchange-correlation functional were used. A plane-wave basis set with a cutoff energy of 30 Ry was employed. We utilized a slab model of a (2  $\times$  2  $\times$  1) supercell containing 8 Ni, 16 O and 8 H to simulate the (0001) surface of hydroxylated NiO (i.

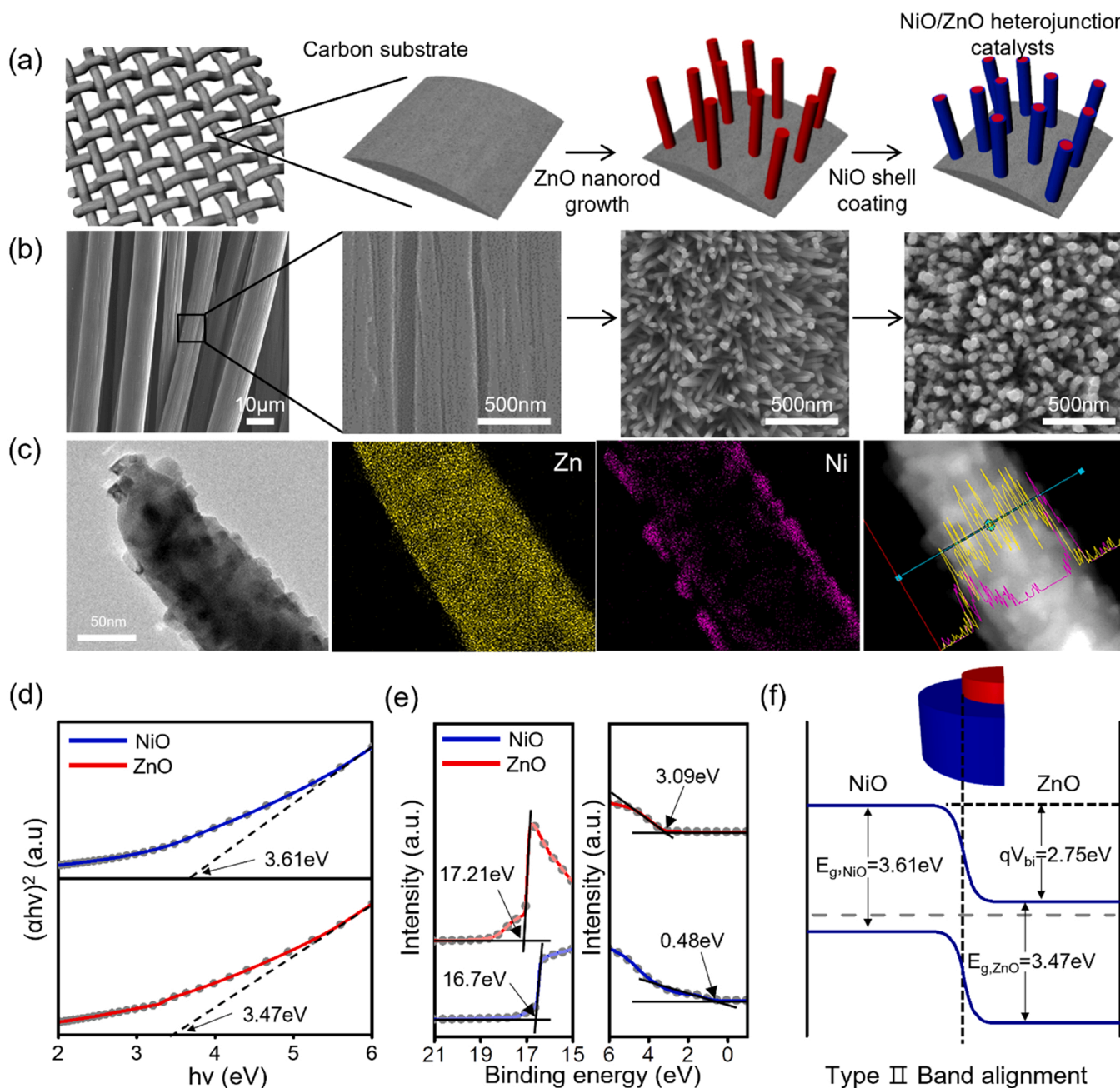


**Fig. 2.** (a) Schematic diagram of the fabrication procedure for NiO/ZnO shell/core nanorods; (b) SEM images corresponding to each step. (c) TEM/EDS images of NiO/ZnO shell/core nanorods. (d) Tauc plots and (e) UPS spectra for NiO and ZnO. (f) Energy level diagram for the NiO/ZnO heterojunction.



e., NiOOH). The k-point set of  $(2 \times 2 \times 1)$  selected by the Monkhorst-Pack scheme was used to obtain Brillouin zone integration. For periodic slab calculations, 2 layers of slabs separated by vacuum layers measuring at least 15 Å were used. For structure optimizations, all ions were relaxed until a maximum force of 0.005 eV/Å was reached.

### 3. Results and discussion

#### 3.1. Formation of heterojunctions in NiO/ZnO catalysts

The fabrication of NiO/ZnO shell/core nanorods is described in Fig. 2a. First, a ZnO nanorod core was formed by hydrothermal synthesis using a  $\text{Zn}(\text{NO}_3)_2$  precursor on a carbon cloth substrate. The diameters of the ZnO nanorods ranged from 40 to 70 nm for 600 nm nanorods (Fig. 2b). Subsequently, the NiO shell was coated by reduction of the  $\text{NiSO}_4$  precursor. The thickness of the NiO shell was approximately 10 nm (Fig. 2b and Fig. S1).

A magnified TEM image of a NiO/ZnO shell/core nanorod and its elemental mapping are shown in Fig. 2c. These results clearly showed the NiO shell and ZnO core structures. The XRD spectrum of the NiO/ZnO nanorod catalyst exhibited peaks at  $37.2^\circ$ ,  $43.2^\circ$ , and  $62.9^\circ$ , corresponding to the (111), (200), and (220) planes of NiO, respectively; peaks at  $31.8^\circ$ ,  $34.4^\circ$  and  $36.2^\circ$  corresponding to the (100), (002) and (101) planes of ZnO were also identified (Fig. S2) [30,31].

We used UV–visible absorption and ultraviolet photoelectron spectroscopies (UPS) to determine the band energy levels for NiO and ZnO. In the Tauc plot shown in Fig. 2d, the extrapolated value to the abscissa of the linear region corresponds to the optical bandgap [32]. The bandgaps of NiO and ZnO were identified as 3.61 eV and 3.47 eV, respectively. The respective values fell within the bandgap ranges of 3.4–4.0 eV and 3.19–3.5 eV seen for NiO and ZnO in previous results [33–35]. In UPS, the cutoff energy for the high energy region corresponded to the work function ( $\Phi$ ), and the onset energy in the low energy region corresponded to the energy difference between the valance band and the Fermi level ( $E_F-E_{VB}$ ). The  $\Phi$  values for NiO and ZnO were

found to be 4.52 eV and 4.02 eV, respectively (Fig. 2e) [36,37]. Additionally, the  $E_F-E_{VB}$  values were 0.48 eV and 3.09 eV, respectively. Using these measurements, an energy level diagram for the NiO/ZnO heterojunction was constructed, as shown in Fig. 2f. The NiO/ZnO junction formed a staggered band arrangement (Type II). In such a heterojunction, the electrons formed by the redox reaction on NiO move rapidly to the ZnO core due to the built-in potential formed at the junction. Subsequently, the electrons also diffuse rapidly within the core along the 1D directional path of the nanorods [38,39].

#### 3.2. Electrochemical methane oxidation at various NiO/ZnO nanorod lengths

We prepared NiO/ZnO nanorod catalysts with various nanorod lengths by controlling the growth time of ZnO. Reactions run for 1 hr, 3 hr, 6 hr, and 9 hr grew nanorods with lengths of 350 nm, 450 nm, 600 nm, and 750 nm, respectively (Fig. 3a). The diameters of these nanorods ranged from 40 to 70 nm.

First, we characterized electrochemical activation of methane by the NiO/ZnO nanorod catalyst with anodic sweep voltammetry. The NiO/ZnO nanorods were applied as catalytic working electrodes, Pt as the counter electrode, and a saturated calomel electrode (SCE) as the reference electrode. A 0.5 M  $\text{Na}_2\text{CO}_3$  aqueous solution was used as the electrolyte. The anodic sweep curves for electrolytes containing methane or nitrogen are compared in Fig. 3b. The peak at 0.8 V<sub>SCE</sub> corresponded to oxidation of  $\text{Ni}^{2+}$  to  $\text{Ni}^{3+}$  on the NiO surface [40–42]. The difference in the curves for methane or nitrogen saturation became apparent above an onset voltage of approximately 0.85 V<sub>SCE</sub>. With methane saturation, the oxidation current density increased significantly; in contrast, no current increase was observed for nitrogen saturation (Fig. S3). These results clearly indicated the oxidation of methane in NiO/ZnO nanorod catalysts under this anodic potential. We observed a NiO/ZnO catalyst electrode and a Pt counter electrode in the 0.85–1 V<sub>SCE</sub> range (Fig. S4). Although vigorous  $\text{H}_2$  bubbles evolved in the Pt electrode, only weak  $\text{O}_2$  production was observed in the NiO/ZnO

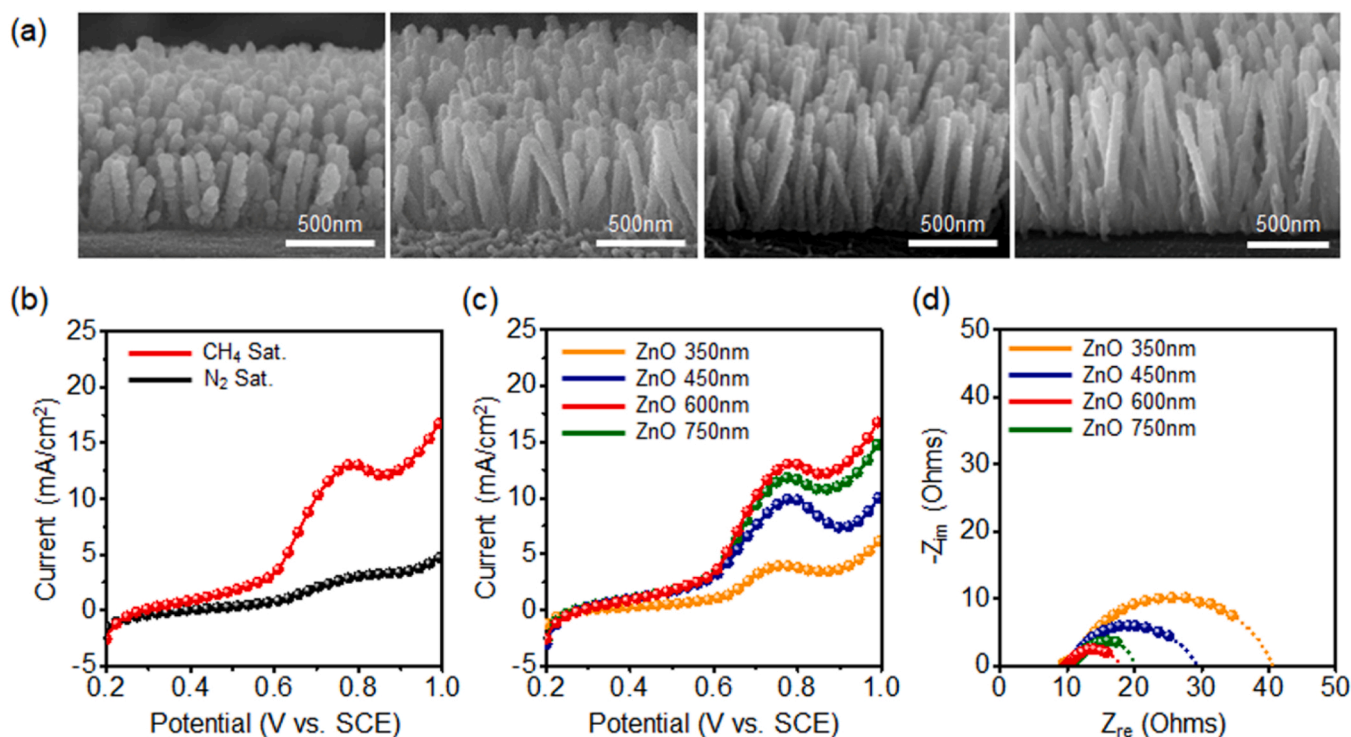


Fig. 3. (a) SEM images of NiO/ZnO nanorod catalysts with lengths of 350 nm, 450 nm, 600 nm and 750 nm. (b) Linear sweep voltammetry curves for NiO/ZnO nanorod catalysts with  $\text{N}_2$  and  $\text{CH}_4$  saturation in the electrolyte. (c) Linear sweep curves and (d) EIS spectra for NiO/ZnO nanorod catalysts of various lengths.

catalytic electrode. This observation suggested that the paired oxidation reaction of the hydrogen evolution reaction is accompanied by the conversion of methane to the liquid product rather than the oxygen evolution reaction.

The NiO/ZnO nanorod catalyst exhibited an oxidation current of  $17 \text{ mA/cm}^2$  at  $1.0 V_{\text{SCE}}$ . Note that this value was significantly higher than the areal current densities measured in electrochemical methane oxidation with various oxide catalysts (Table S1); even considering differences in catalytic composition, the distinctly high current density may reveal significantly enhanced electron transport in the NiO/ZnO heterojunction structure.

Then, we compared electrochemical methane activation with NiO/ZnO nanorod catalysts of various lengths. The curves of  $V_{\text{SCE}}$  versus areal current density for these NiO/ZnO nanorod catalysts are shown in Fig. 3c. As the lengths of the nanorods increased, the areal current density for methane oxidation increased. The 600 nm nanorod catalyst exhibited the highest current density. As the nanorods were lengthened, the surface area of the nanorods increased, thereby increasing the areal

current density. However, for the 750 nm nanorod catalyst, the current density was reduced. To analyze the difference in activity according to the nanorod length, we compared the electrochemical active areas of 350 nm, 600 nm and 750 nm nanorod catalysts by cyclic voltammetry (Fig. S5). The 600 nm nanorods catalyst exhibited about 2.5 times higher the active area compared to the 350 nm nanorods, however, the 750 nm nanorods exhibited about a 15 % reduction in the active area compared to the 600 nm nanorods. This result suggests that the methane oxidation activity is closely related to the electrochemically active area. In particular, the decrease in oxidation current in the 750 nm nanorod catalyst compared to the 600 nm nanorod catalyst is due to the decrease in the electrochemically active area. To rationalize this result, we present the deterioration of ion access due to agglomeration by significant small nanorods at 750 nm nanorods (Fig. S6).

The Nyquist plots obtained with electrochemical impedance spectroscopy (EIS) for these nanorod catalysts of various lengths are presented in Fig. 3d. The semicircle in the 0.1–1.0 MHz range represents the charge transport resistance across the catalyst surface [43]. The

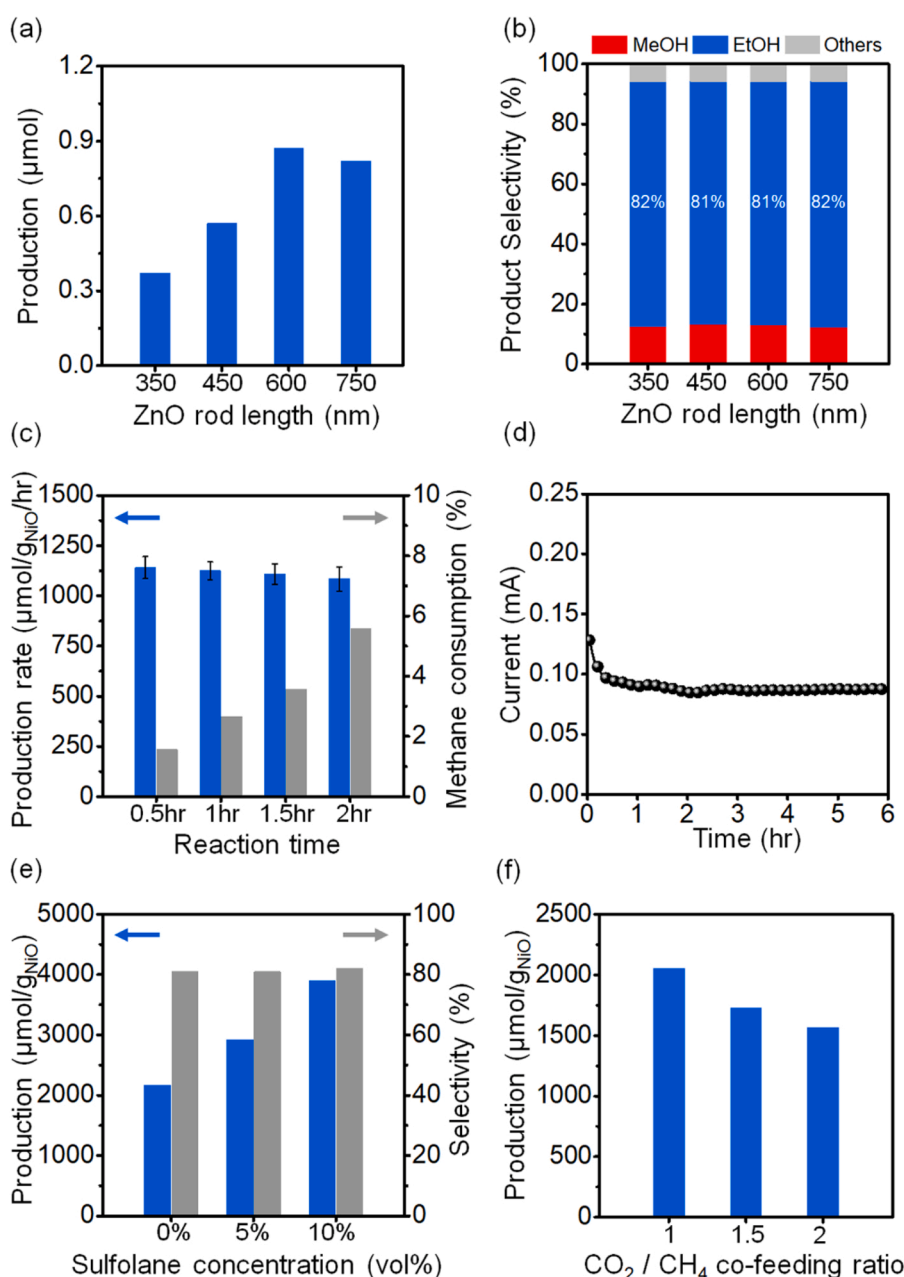


**Fig. 4.** (a) Ethanol productivity in methane conversion and (b) selectivity for oxygenates with NiO/ZnO nanorod catalysts of various lengths. (c) Production rates for ethanol during 0.5, 1, 1.5 and 2 hr reactions with 600 nm NiO/ZnO nanorod catalysts. (d) Oxidation current for the 600 nm NiO/ZnO nanorod catalyst for a 6 hr reaction. Ethanol production and selectivity on a 600 nm NiO/ZnO nanorod catalyst (e) with incorporation of sulfane in the electrolyte and (f) from a CO<sub>2</sub>/CH<sub>4</sub> feed mixture for a 2 hr reaction.

resistance values analyzed with the equivalent circuit decreased as the lengths of the nanorods increased to 600 nm but increased slightly for the 750 nm nanorods. This result corresponded well with the result of the methane oxidation current with increasing the length of the nanorod catalyst. In particular, this result confirmed the deterioration of the electrochemical reaction kinetics in the agglomerated 750 nm nanorod catalyst.

### 3.3. Analysis of methane conversion products

We analyzed the methane oxidation products from the NiO/ZnO nanorod catalysts. These experiments were performed by applying a potential of 1.5 V<sub>Pt</sub> in a two-electrode reactor with Pt as the reference electrode. A potential of 1.5 V<sub>Pt</sub> is equivalent to 0.9–1.0 V<sub>SCE</sub> (Fig. S7). The productivities for electrochemical methane conversion by nanorod catalysts of various lengths are compared in Fig. 4a. For all catalysts, ethanol was identified as the main product. For the 350–600 nm nanorods, ethanol production increased proportionally with nanorod length, but the 750 nm nanorods exhibited decreased production. This result is highly consistent with the oxidation current analysis. As the nanorod lengths increased, the increased catalyst surface area increased production, but the decrease in effective surface area due to agglomeration in the long nanorods decreased production. The 600-nm nanorod catalyst showed the highest ethanol production of 2168.5 μmol/g<sub>NiO</sub> for a 2 hr reaction. The Faraday efficiency (FE), the proportion of supplied charge used in the methane-ethanol conversion, was 61 % [16].

The selectivity for liquid oxygenates in these NiO/ZnO nanorod catalysts is shown in Fig. 4b. The product selectivity was similar for nanorod catalysts of various lengths. The selectivities of the 600 nm nanorod catalyst for ethanol and methanol production were 81 % and 13 %, respectively. Other oxygenates included mainly acetone. Later, the analysis of the reaction mechanism confirmed that a high selectivity to ethanol was obtained by favorable deprotonation of the adsorbed methanol. The rates for production of ethanol by the 600 nm nanorod catalysts during reaction times of 0.5, 1, 1.5, and 2 hr are displayed in Fig. 4c. The production rates during the 2 hr reactions exhibited an average of 1084.2 μmol/g NiO/hr and stable conversion with a reduction of less than 5 %. The production rates for the NiO/ZnO nanorod catalysts are superior to those achieved with recently reported electrochemical catalysts (Table S2). In Fig. 4d, the oxidation currents measured during 6 hr reactions are displayed; the currents exhibited operational stability with only a 10 % decrease in the stabilized conversion reaction region after 10 min.

The low solubility of methane in aqueous solutions constitutes an obstacle to methane conversion. We added sulfolane to the electrolyte to enhance methane solubility. Methane has a high solubility of 78.93 mg/L in sulfolane at room temperature and pressure [44], which is approximately 3.5 times higher than its solubility in water. We proceeded with the reaction by saturating methane in 5 % v/v and 10 % v/v sulfolane/water mixtures. The ethanol production rates for 5 % and 10 % sulfolane/water were 2918.5 μmol/g<sub>NiO</sub> and 3896.7 μmol/g<sub>NiO</sub>, respectively, which were improved by 35 % and 80 % compared to the sulfolane-free electrolyte, respectively (Fig. 4e). The ethanol selectivities of the reactions were 80.9 % and 82 %, respectively, similar to that for the reaction with pure electrolyte.

Practical methane evolution is often accompanied by significant CO<sub>2</sub> production. Biogas from anaerobic digestion typically contains significant CO<sub>2</sub> (30–60 %) with methane as the main constituent [45]. Landfill gas also contains significant CO<sub>2</sub> (40–60 %) along with methane [46]. We demonstrated electrochemical methane conversion with direct utilization of CO<sub>2</sub>. CO<sub>2</sub> was oxidized to the CO<sub>3</sub><sup>2-</sup> anion by an acid dissociation reaction occurring at pHs above 10, which generates CO<sub>3</sub><sup>2-</sup> in situ [47,48]. We conducted the conversion by feeding CH<sub>4</sub> and CO<sub>2</sub> together with CO<sub>2</sub>/CH<sub>4</sub> ratios of 1–2 (Fig. 4f). We successfully achieved an ethanol production rate of 2054.3 μmol/g<sub>NiO</sub> for CO<sub>2</sub>/CH<sub>4</sub> = 1. For gas ratios of 1.5 and 2, the ethanol production rate decreased, which was

attributed to the relatively low supply of methane.

### 3.4. Mechanisms for electrochemical methane conversion

We analyzed the products of methane oxidation by using isotopically labeled reactants. The NMR spectrum of the liquid products obtained from the reaction using <sup>13</sup>C-labeled CH<sub>4</sub> is presented in Fig. 5a; the spectrum shows <sup>13</sup>C-labeled ethanol and methanol. The GC-MS spectrum of the products prepared using <sup>18</sup>O-labeled CO<sub>3</sub><sup>2-</sup> is presented in Fig. 5b. The GC-MS analysis shows shifts of 2 *m/z* in the peaks for ethanol. The shifted peaks corresponded to ethanol containing <sup>18</sup>O. The intensity ratio of the ethanol peak and the <sup>18</sup>O-ethanol peak was 2:1, which is consistent with the C<sup>16</sup>O<sub>3</sub><sup>2-</sup>:C<sup>18</sup>O<sub>3</sub><sup>2-</sup> ratio used in the reaction. These isotopic results revealed the overall reaction in which ethanol was produced by oxidation of methane by oxygen in CO<sub>3</sub><sup>2-</sup>. Meanwhile, the GC-MS analysis in the reaction with H<sub>2</sub><sup>18</sup>O did not detect isotope-labeled ethanol, confirming that methane oxidation does not proceed by oxygen formed by electrochemical water splitting (Fig. S8).

We proposed a thermodynamically favorable reaction pathway for the electrochemical methane-ethanol conversion on NiO/ZnO nanorod catalysts (Fig. S9). First, adsorption of CO<sub>3</sub><sup>2-</sup> on the catalyst surface generates active oxygen (CO<sub>3</sub><sup>2-</sup> (ads) → CO<sub>2</sub> (g) + O (ads) + 2e<sup>-</sup>). The dissociation of the adsorbed CO<sub>3</sub><sup>2-</sup> was confirmed by the component analysis of the gas phase in the reactor; we detected CO<sub>2</sub>(g) only under the electrochemical potential, confirming that the CO<sub>3</sub><sup>2-</sup> dissociation proceeded electrochemically (Fig. 5c). In addition, the active oxygen on the catalyst surface was confirmed by XPS analysis. We measured the O 1s XPS of a NiO/ZnO nanorod catalyst with an applied oxidation potential in a CO<sub>3</sub><sup>2-</sup> electrolyte (Fig. 5d). The O 1s spectrum was deconvoluted to give peaks at 529.1 eV, 531 eV, and 532.4 eV, which corresponded to lattice oxygen, surface oxygen, and adsorbed oxygen, respectively [49]. The catalyst with applied potential exhibited a significant increase in the adsorbed oxygen peak, which corresponds to the electrochemically promoted active oxygen (Fig. 5d).

Methane is activated by the O (ads) to produce methanol (CH<sub>4</sub> + O (ads) → CH<sub>3</sub>OH (ads)) (Fig. S9). Methanol was observed in the <sup>13</sup>C NMR spectrum and was also detected in the reaction using C<sup>18</sup>O<sub>3</sub><sup>2-</sup> (Fig. 5a and Fig. S10). Note, however, that desorption to methanol (CH<sub>3</sub>OH(ads) → CH<sub>3</sub>OH (l)) is an unfavorable endothermic process with an energy change of about 0.06 eV (Fig. S9). Indeed, we observed low selectivity to methanol in the measurement of the production rate (Fig. 4b). The unfavorable desorption of methanol promotes further reaction of the adsorbed methanol.

The adsorbed methanol is dehydrogenated (CH<sub>3</sub>OH (ads) → CH<sub>2</sub>O (ads) + 2H<sup>+</sup> + 2e<sup>-</sup>) (Fig. S9). Krewer and co-workers have also proposed the formation of CH<sub>3</sub>O and additional CH<sub>2</sub>O in the electrochemical dehydrogenation of CH<sub>3</sub>OH [50]. In the energy diagram, the formation of CH<sub>3</sub>O was confirmed as an exothermic process. Subsequent formation of CH<sub>2</sub>O exhibited a limiting step with an energy change of 0.49 eV; However, this process proceeds in an electrochemical pathway, and thus can be overcome by application of an anode potential (above about 0.5 V<sub>SCE</sub>). These dehydrogenated species were identified in XPS C 1s analysis (Fig. S11).

Finally, CH<sub>2</sub>O undergoes a coupling reaction with methane to produce ethanol (CH<sub>2</sub>O (ads) + CH<sub>4</sub> → CH<sub>3</sub>CH<sub>2</sub>OH). The C of the deprotonated CH<sub>2</sub>O is electropositive and thus binds directly to CH<sub>4</sub> [15]. The ethanol is stable against further oxidation, presumably due to solvation [50]; no oxygenate products were detected in the electrochemical reaction of ethanol (Fig. S12). This result also supports the high selectivity of ethanol in the conversion (Table 1).

## 4. Conclusion

We demonstrated a NiO/ZnO nanorod catalyst used to obtain high-productivity electrochemical methane conversion. Heterojunction nanorods allowed fast charge transfer by built-in dislocation and

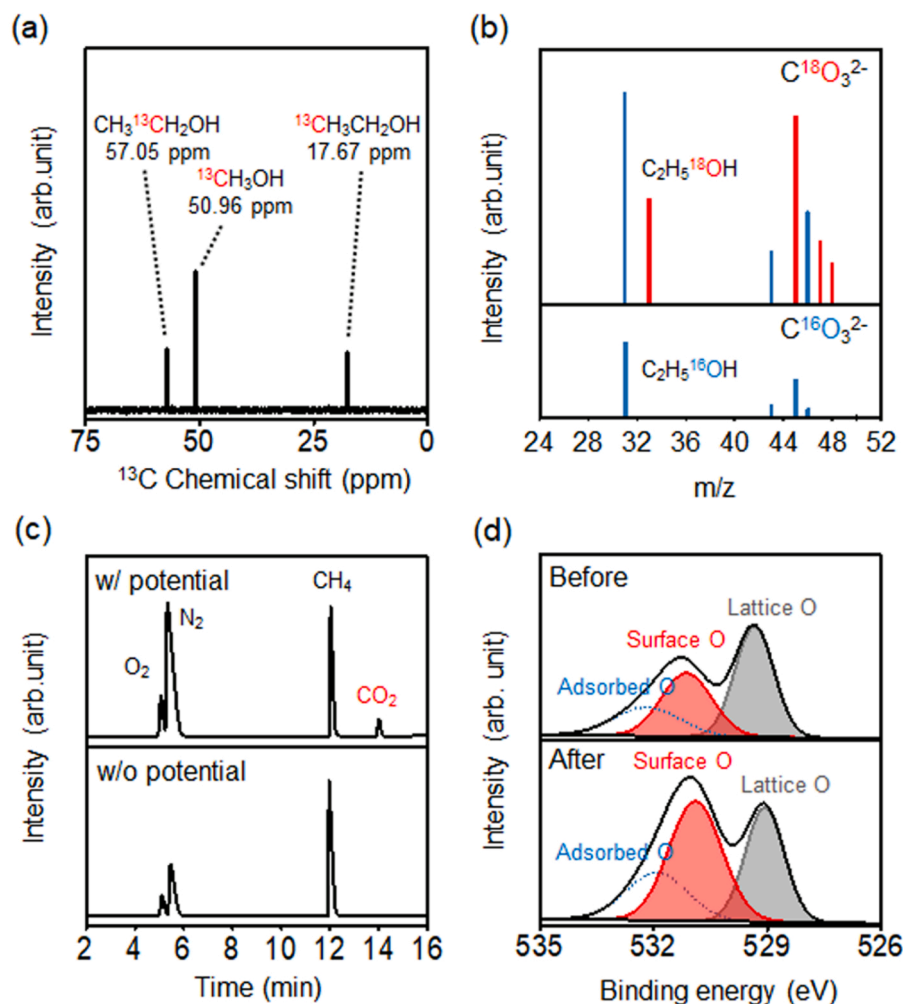


**Fig. 5.** (a)  $^{13}\text{C}$  NMR spectrum of the product obtained using  $^{13}\text{CH}_4$ . (b) MS spectrum for the ethanol product in  $^{18}\text{CO}_3^{2-}$  containing electrolyte; typical MS spectrum for ethanol. (c) Gas chromatogram for gaseous products formed with and without application of a potential. (d) O 1s XPS spectrum of the NiO/ZnO nanorod catalyst with and without application of a potential.

**Table 1**

Electrochemical methane conversion with NiO/ZnO nanorod catalysts of various lengths and over various reaction times.

Entry	NiO/ZnO nanorod catalyst length	Reaction Time (hr)	Amount of product ( $\mu\text{mol}\cdot\text{g}_{\text{cat}}^{-1}$ )			$\text{CH}_3\text{CH}_2\text{OH}$ productivity ( $\mu\text{mol}\cdot\text{g}_{\text{cat}}^{-1}\cdot\text{hr}^{-1}$ )
			$\text{CH}_3\text{OH}$	$\text{C}_2\text{H}_5\text{OH}$	Others	
1	350 nm	2	312.5	2029.0	143.5	1014.5
2	450 nm	2	347.2	2101.4	153.0	1050.7
3	600 nm	2	351.6	2168.5	155.0	1084.2
4	750 nm	2	297.3	2004.2	138.6	1002.1
5	600 nm	0.5	140.6	570.7	103.3	1141.3
6	600 nm	1	257.8	1125.0	116.2	1125
7	600 nm	1.5	304.7	1663.0	142.0	1108.7

Test conditions: Temperature = room temperature, Electrolyte = 0.5 M  $\text{Na}_2\text{CO}_3$ ,  $\text{CH}_4$  pressure = 1 bar, applied potential = 1.5 V.

vectorial diffusion pathways, thereby promoting the electrochemical conversion. The NiO/ZnO nanorod catalyst was prepared via growth of ZnO nanorods, followed by coating with the NiO catalyst shell. Measurements of the bandgap and valence band levels confirmed the staggered band arrangement at the NiO/ZnO junction. We found the highest methane oxidation current and consequently high methane-ethanol conversion with the 600 nm long nanorod catalyst. At longer nanorod lengths, conversion was inhibited by a decrease in the effective surface area due to agglomeration between the nanorods. The 600 nm NiO/ZnO nanorod catalyst achieved ethanol productivity of  $1084.2 \mu\text{mol}/\text{g}_{\text{NiO}}/\text{hr}$  with a selectivity of 81 %. We applied a sulfolane/water mixture as an

electrolyte solvent to improve methane conversion. Due to the high methane solubility in sulfolane, the methane-ethanol conversion was improved by 80 %. Additionally, we used a  $\text{CH}_4/\text{CO}_2$  gas mixture to perform electrochemical conversion; significant proportions of  $\text{CO}_2$  are often produced in practical methane-generating environments. We demonstrated successful methane oxidation with conversion of  $\text{CO}_2$  to  $\text{CO}_3^{2-}$  anions in a high pH environment. The conversion of methane to ethanol was confirmed by isotopic labelling. We presented a favorable reaction mechanism involving formation of active oxygen by adsorption of the  $\text{CO}_3^{2-}$  anion, activation of methane by active oxygen (formation of methanol), deprotonation of methanol, and production of ethanol by



coupling with methane. Our study highlights the importance of electronic band engineering for catalysts used in electrochemical methane oxidation.

### CRedit authorship contribution statement

**Cheolho Kim:** Investigation, Validation, Theoretical simulation, Writing – original draft. **Heewon Min:** Investigation, Formal analysis, Data curation. **Junmin Kim:** Investigation, Formal analysis, Data curation. **Jiwon Sul:** Investigation, Formal analysis, Data curation. **Jiwoo Yang:** Investigation, Formal analysis, Data curation. **Jun Hyuk Moon:** Conceptualization, Funding, acquisition, Supervision, Project administration, Writing – review & editing.

### Declaration of Competing Interest

The authors declare that they have no known competing financial interests or personal relationships that could have appeared to influence the work reported in this paper.

### Data Availability

Data will be made available on request.

### Acknowledgements

This work was supported by National Research Foundation of Korea (Grant No. 2022R1A2C2005228, 2021M3D3A1A01022112). The Korea Basic Science Institute is also acknowledged for the SEM and XPS measurements.

### Appendix A. Supporting information

Supplementary data associated with this article can be found in the online version at [doi:10.1016/j.apcatb.2022.122129](https://doi.org/10.1016/j.apcatb.2022.122129).

### References

- [1] X. Yu, V. De Waele, A. Löfberg, V. Ordonsky, A.Y. Khodakov, Selective photocatalytic conversion of methane into carbon monoxide over zinc-heteropolyacid-titania nanocomposites, *Nat. Commun.* 10 (2019) 1–10.
- [2] Y. Yu, X.-w. ZHANG, J.-W. Liu, Y. Lee, X. Li, Natural gas hydrate resources and hydrate technologies: a review and analysis of the associated energy and global warming challenges, *Energy Environ. Sci.* (2021).
- [3] X. Meng, X. Cui, N.P. Rajan, L. Yu, D. Deng, X. Bao, Direct methane conversion under mild condition by thermo-, electro-, or photocatalysis, *Chem* 5 (2019) 2296–2325.
- [4] P. Schwach, X. Pan, X. Bao, Direct conversion of methane to value-added chemicals over heterogeneous catalysts: challenges and prospects, *Chem. Rev.* 117 (2017) 8497–8520.
- [5] M. Li, J. Shan, G. Giannakakis, M. Ouyang, S. Cao, S. Lee, L.F. Allard, M. Flytzani-Stephanopoulos, Single-step selective oxidation of methane to methanol in the aqueous phase on iridium-based catalysts, *Appl. Catal. B-Environ.* 292 (2021), 120124.
- [6] T. Moteki, N. Tominaga, M. Ogura, Mechanism investigation and product selectivity control on CO-assisted direct conversion of methane into C1 and C2 oxygenates catalyzed by zeolite-supported Rh, *Appl. Catal. B-Environ.* 300 (2022), 120742.
- [7] K. Zhu, S. Liang, X. Cui, R. Huang, N. Wan, L. Hua, H. Li, H. Chen, Z. Zhao, G. Hou, Highly efficient conversion of methane to formic acid under mild conditions at ZSM-5-confined Fe-sites, *Nano Energy* 82 (2021), 105718.
- [8] S. Yuan, Y. Li, J. Peng, Y.M. Questell-Santiago, K. Akkiraju, L. Giordano, D. J. Zheng, S. Bagi, Y. Román-Leshkov, Y. Shao-Horn, Conversion of methane into liquid fuels—bridging thermal catalysis with electrocatalysis, *Adv. Energy Mater.* 10 (2020), 2002154.
- [9] Y. Xu, D. Wu, P. Deng, J. Li, J. Luo, Q. Chen, W. Huang, C.M. Shim, C. Jia, Z. Liu, Au decorated Pd nanowires for methane oxidation to liquid C1 products, *Appl. Catal. B-Environ.* 308 (2022), 121223.
- [10] J.J. Spivey, A. Egebebi, Heterogeneous catalytic synthesis of ethanol from biomass-derived syngas, *Chem. Soc. Rev.* 36 (2007) 1514–1528.
- [11] X. Guo, G. Fang, G. Li, H. Ma, H. Fan, L. Yu, C. Ma, X. Wu, D. Deng, M. Wei, Direct, nonoxidative conversion of methane to ethylene, aromatics, and hydrogen, *Science* 344 (2014) 616–619.
- [12] P. Tomkins, M. Ranocchiari, J.A. van Bokhoven, Direct conversion of methane to methanol under mild conditions over Cu-zeolites and beyond, *Acc. Chem. Res.* 50 (2017) 418–425.
- [13] E.V. Starokon, M.V. Parfenov, L.V. Pirutko, S.I. Abornev, G.I. Panov, Room-temperature oxidation of methane by  $\alpha$ -oxygen and extraction of products from the FeZSM-5, *Surf., J. Phys. Chem. C.* 115 (2011) 2155–2161.
- [14] S.J. Freakley, N. Dimitratos, D.J. Willock, S.H. Taylor, C.J. Kiely, G.J. Hutchings, Methane oxidation to methanol in water, *Acc. Chem. Res.* 54 (2021) 2614–2623.
- [15] N. Spinner, W.E. Mustain, Electrochemical methane activation and conversion to oxygenates at room temperature, *J. Electrochem. Soc.* 160 (2013) F1275.
- [16] Y. Song, Y. Zhao, G. Nan, W. Chen, Z. Guo, S. Li, Z. Tang, W. Wei, Y. Sun, Electrocatalytic oxidation of methane to ethanol via NiO/Ni interface, *Appl. Catal. B-Environ.* 270 (2020), 118888.
- [17] Z. Xie, M. Chen, Y. Chen, A. Guan, Q. Han, G. Zheng, Electrocatalytic methane oxidation to ethanol via Rh/ZnO nanosheets, *J. Phys. Chem. C.* 125 (2021) 13324–13330.
- [18] J. Lee, J. Yang, J.H. Moon, Solar cell-powered electrochemical methane-to-methanol conversion with CuO/CeO2 catalysts, *ACS Energy Lett.* 6 (2021) 893–899.
- [19] N. Xu, C.A. Coco, Y. Wang, T. Su, Y. Wang, L. Peng, Y. Zhang, Y. Liu, J. Qiao, X.-D. Zhou, Electro-conversion of methane to alcohols on “capsule-like” binary metal oxide catalysts, *Appl. Catal. B-Environ.* 282 (2021), 119572.
- [20] A. Prajapati, B.A. Collins, J.D. Goodpaster, M.R. Singh, Fundamental insight into electrochemical oxidation of methane towards methanol on transition metal oxides, *Proc. Natl. Acad. Sci.* 118 (2021).
- [21] M. Ravi, M. Ranocchiari, J.A. van Bokhoven, The direct catalytic oxidation of methane to methanol—a critical assessment, *Angew. Chem. Int. Ed.* 56 (2017) 16464–16483.
- [22] R.C. Rizzo, T. Aynechi, D.A. Case, I.D. Kuntz, Estimation of absolute free energies of hydration using continuum methods: accuracy of partial charge models and optimization of nonpolar contributions, *J. Chem. Theory Comput.* 2 (2006) 128–139.
- [23] C. Oh, J. Kim, Y.J. Hwang, M. Ma, J.H. Park, Electrocatalytic methane oxidation on Co3O4-incorporated ZnO nanotube powder, *Appl. Catal. B-Environ.* 283 (2021), 119653.
- [24] Y. Kang, Z. Li, X. Lv, W. Song, Y. Wei, X. Zhang, J. Liu, Z. Zhao, Active oxygen promoted electrochemical conversion of methane on two-dimensional carbide (MXenes): From stability, reactivity and selectivity, *J. Catal.* 393 (2021) 20–29.
- [25] K. Wang, D. Liu, P. Deng, L. Liu, S. Lu, Z. Sun, Y. Ma, Y. Wang, M. Li, B.Y. Xia, Band alignment in Zn2SnO4/SnO2 heterostructure enabling efficient CO2 electrochemical reduction, *Nano Energy* 64 (2019), 103954.
- [26] Y. Zeng, Z. Cao, J. Liao, H. Liang, B. Wei, X. Xu, H. Xu, J. Zheng, W. Zhu, L. Cavallo, Construction of hydroxide pn junction for water splitting electrocatalysis, *Appl. Catal. B-Environ.* 292 (2021), 120160.
- [27] X. Zhang, S.D. House, Y. Tang, L. Nguyen, Y. Li, A.A. Opalade, J.C. Yang, Z. Sun, F. Tao, Complete oxidation of methane on NiO nanoclusters supported on CeO2 nanorods through synergistic effect, *ACS Sustain. Chem. Eng.* 6 (2018) 6467–6477.
- [28] D. Delgado, B. Solsona, A. Ykrel, A. Rodríguez-Gómez, A. Caballero, E. Rodríguez-Aguado, E. Rodríguez-Castellón, J.M. López Nieto, Redox and catalytic properties of promoted NiO catalysts for the oxidative dehydrogenation of ethane, *J. Phys. Chem. C.* 121 (2017) 25132–25142.
- [29] X. Zhao, Q. Li, L. Xu, Z. Zhang, Z. Kang, Q. Liao, Y. Zhang, Interface engineering in 1D ZnO-based heterostructures for photoelectrical devices, *Adv. Funct. Mater.* 32 (2022), 2106887.
- [30] M. Kanthimathi, A. Dhathathreyan, B. Nair, Nanosized nickel oxide using bovine serum albumin as template, *Mater. Lett.* 58 (2004) 2914–2917.
- [31] V. Dinesh, P. Bijl, A. Ashok, S. Dhara, M. Kamruddin, A. Tyagi, B. Raj, Plasmon-mediated, highly enhanced photocatalytic degradation of industrial textile dyes using hybrid ZnO@Ag core-shell nanorods, *RSC Adv.* 4 (2014) 58930–58940.
- [32] K. He, T. Tadesse Tsega, X. Liu, J. Zai, X.H. Li, X. Liu, W. Li, N. Ali, X. Qian, Utilizing the Space-Charge Region of the FeNi-LDH/CoP p-n Junction to Promote Performance in Oxygen Evolution Electrocatalysis, *Angew. Chem. Int. Ed.* 58 (2019) 11903–11909.
- [33] N. Alidoust, M.C. Toroker, J.A. Keith, E.A. Carter, Significant reduction in NiO band gap upon formation of LiNi1–xO alloys: applications to solar energy conversion, *ChemSusChem* 7 (2014) 195–201.
- [34] M.T. Uddin, Y. Nicolas, C. Olivier, W. Jaegermann, N. Rockstroh, H. Junge, T. Toupance, Band alignment investigations of heterostructure NiO/TiO2 2D nanomaterials used as efficient heterojunction earth-abundant metal oxide photocatalysts for hydrogen production, *Phys. Chem. Chem. Phys.* 19 (2017) 19279–19288.
- [35] N. Kamarulzaman, M.F. Kasim, R. Rusdi, Band gap narrowing and widening of ZnO nanostructures and doped materials, *Nanoscale Res. Lett.* 10 (2015) 1–12.
- [36] S. Pansri, R. Supruangnet, H. Nakajima, S. Rattanasuporn, S. Noothongkaew, Band offset determination of p-NiO/n-TiO2 heterojunctions for applications in high-performance UV photodetectors, *J. Mater. Sci.* 55 (2020) 4332–4344.
- [37] E. Zheng, Y. Wang, J. Song, X.-F. Wang, W. Tian, G. Chen, T. Miyasaka, ZnO/ZnS core-shell composites for low-temperature-processed perovskite solar cells, *J. Energy Chem.* 27 (2018) 1461–1467.
- [38] J. Li, F. Zhao, L. Zhang, M. Zhang, H. Jiang, S. Li, J. Li, Electrospun hollow ZnO/NiO heterostructures with enhanced photocatalytic activity, *RSC Adv.* 5 (2015) 67610–67616.
- [39] Y. Mao, Y. Cheng, J. Wang, H. Yang, M. Li, J. Chen, M. Chao, Y. Tong, E. Liang, Amorphous NiO electrocatalyst overcoated ZnO nanorod photoanodes for enhanced photoelectrochemical performance, *N. J. Chem.* 40 (2016) 107–112.



- [40] K. Han, Y. Liu, H. Huang, Q. Gong, Z. Zhang, G. Zhou, Tremella-like NiO microspheres embedded with fish-scale-like polypyrrole for high-performance asymmetric supercapacitor, *RSC Adv.* 9 (2019) 21608–21615.
- [41] K. Han, H. Huang, Q. Gong, T. Si, Z. Zhang, G. Zhou, Temperature-induced hierarchical Tremella-like and Pinecone-like NiO microspheres for high-performance supercapacitor electrode materials, *J. Mater. Sci.* 53 (2018) 12477–12491.
- [42] J. Yang, M. Ma, C. Sun, Y. Zhang, W. Huang, X. Dong, Hybrid NiCo<sub>2</sub>S<sub>4</sub>@MnO<sub>2</sub> heterostructures for high-performance supercapacitor electrodes, *J. Mater. Chem. A* 3 (2015) 1258–1264.
- [43] V.D. Silva, T.A. Simoes, J.P. Grilo, E.S. Medeiros, D.A. Macedo, Impact of the NiO nanostructure morphology on the oxygen evolution reaction catalysis, *J. Mater. Sci.* 55 (2020) 6648–6659.
- [44] A. Henni, P. Tontiwachwuthikul, A. Chakma, Solubility study of methane and ethane in promising physical solvents for natural gas sweetening operations, *J. Chem. Eng. Data* 51 (2006) 64–67.
- [45] M. Zeppilli, D. Pavesi, M. Gottardo, F. Micolucci, M. Villano, M. Majone, Using effluents from two-phase anaerobic digestion to feed a methane-producing microbial electrolysis, *Chem. Eng. J.* 328 (2017) 428–433.
- [46] R. Gao, C. Zhang, Y.-J. Lee, G. Kwak, K.-W. Jun, S.K. Kim, H.-G. Park, G. Guan, Sustainable production of methanol using landfill gas via carbon dioxide reforming and hydrogenation: process development and techno-economic analysis, *J. Clean. Prod.* 272 (2020), 122552.
- [47] D.A. Henckel, M.J. Counihan, H.E. Holmes, X. Chen, U.O. Nwabara, S. Verma, J. Rodríguez-López, P.J. Kenis, A.A. Gewirth, Potential dependence of the local pH in a CO<sub>2</sub> reduction electrolyzer, *ACS Catal.* 11 (2020) 255–263.
- [48] C. Kim, J. Kim, S. Joo, Y. Bu, M. Liu, J. Cho, G. Kim, Efficient CO<sub>2</sub> utilization via a hybrid Na-CO<sub>2</sub> system based on CO<sub>2</sub> dissolution, *Iscience* 9 (2018) 278–285.
- [49] Z. Xiao, Y.-C. Huang, C.-L. Dong, C. Xie, Z. Liu, S. Du, W. Chen, D. Yan, L. Tao, Z. Shu, Operando identification of the dynamic behavior of oxygen vacancy-rich Co<sub>3</sub>O<sub>4</sub> for oxygen evolution reaction, *J. Am. Chem. Soc.* 142 (2020) 12087–12095.
- [50] A.A. Latimer, A. Kakekhani, A.R. Kulkarni, J.K. Nørskov, Direct methane to methanol: the selectivity–conversion limit and design strategies, *ACS Catal.* 8 (2018) 6894–6907.